Bioconjugate Chemistry

Article

Cite This: Bioconjugate Chem. 2019, 30, 1711−1723

pubs.acs.org/bc

An Albumin Sandwich Enhances in Vivo Circulation and Stability of Metabolically Labile Peptides

Rui Tian,[†,‡] Shoujun Zhu,[*,‡] Qiao Zeng,[§] Lixin Lang,[‡] Ying Ma,[‡] Dale O. Kiesewetter,[‡] Yi Liu,[‡] Xiao Fu,[‡] Joseph Lau,[‡] Guizhi Zhu,[‡] Orit Jacobson,[‡] Zhantong Wang,[‡] Yunlu Dai,[‡] Guocan Yu,[‡] Bernard R. Brooks,[§] Gang Liu,[†] Gang Niu,[*,‡] and Xiaoyuan Chen[*,‡]

[†]State Key Laboratory of Molecular Vaccinology and Molecular Diagnostics & Center for Molecular Imaging and Translational Medicine, School of Public Health, Xiamen University, Xiamen 361102, China

[‡]Laboratory of Molecular Imaging and Nanomedicine, National Institute of Biomedical Imaging and Bioengineering (NIBIB), and [§]Laboratory of Computational Biology, National Heart, Lung and Blood Institute, National Institutes of Health (NIH), Bethesda, Maryland 20892, United States

Supporting Information

ABSTRACT: The effectiveness of numerous molecular drugs is hampered by their poor pharmacokinetics. Different from previous approaches with limited effectiveness, most recently, emerging high-affinity albumin binding moieties (ABMs) for in vivo hitchhiking of endogenous albumin opens up an avenue to chaperone small molecules for long-acting therapeutics. Although several FDA-approved fatty acids have shown prolonged residence and therapeutic effect, an easily synthesized, water-soluble, and high-efficiency ABM with versatile drug loading ability is urgently needed to improve the therapeutic efficacy of short-lived constructs. We herein identified an ideal bivalent Evans blue derivative, denoted as $N(tEB)_2$, as a smart ABM-delivery platform to chaperone short-lived molecules, through both computational modeling screening and efficient synthetic schemes. The optimal $N(tEB)_2$ could reversibly link two molecules of albumin through its two binding heads with a preferable spacer, resulting in significantly extended circulation half-life of a preloaded cargo and water-soluble. Notably, this in situ dimerization of albumin was able to sandwich peptide therapeutics to protect them from proteolysis. As an application, we conjugated $N(tEB)_2$ with exendin-4 for long-acting glucose control in a diabetic mouse model, and it was superior to both previously tested NtEB-exendin-4 (Abextide) and the newly FDA-approved semaglutide, which has been arguably the best commercial weekly formula so far. Hence, this novel albumin binder has excellent clinical potential for next-generation biomimetic drug delivery systems.

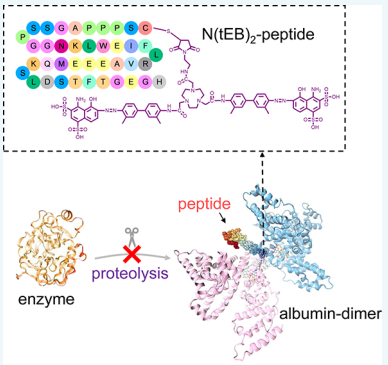

INTRODUCTION

Human serum albumin (HSA) has been used as a drug carrier for decades, due to its abundance (35−50 mg/mL) in blood and long systemic circulation.[1,2] The most popular strategy to "hitchhike" albumin is to link a drug candidate with an albumin binding moiety (ABM) so that the conjugate binds to circulating albumin in situ.[3−6] Several FDA approved drugs incorporate fatty acids as ABMs. However, these fatty acid conjugates tend to have high propensity to accumulate in the liver. The lipophilic nature also increases the difficulty of chemical synthesis and production of these drugs;[7−9] hence, most of these kinds of ABMs have been administered subcutaneously for diabetes treatment or vaccination.[10] While other endogenous and exogenous molecules can also bind albumin, a majority of them cannot be used as ABMs because of reduced binding affinity to albumin upon chemical modification.[11] Researchers have used DNA-encoded chemical library[12] and phage display[13] to identify conjugatable ABMs (i.e., 4-(*p*-iodophenyl) butyric acid derivatives). However, the application of these ABMs has been limited by moderate improvements in the pharmacokinetics of the conjugates or by the mismatch between ABM and drug load.[14−17] Therefore, an ABM with versatile drug loading ability is still needed to improve drug delivery.

Evans Blue (EB) dye is an important tool for physiology and pathology, especially for assessing integrity of blood-brain barrier and vascular permeability, because of its strong affinity for albumin.[18−20] Our lab developed a series of truncated Evans Blue (tEB) derivates as ABMs for various applications, ranging from blood pool imaging,[21] lymphatic imaging,[22] tumor vaccination,[6] radioligand therapy,[15,23−25] to antidiabetic treatment.[26,27] However, in truncating EB we reduced its binding affinity for albumin, which would further weaken the pharmacokinetics. Hence, we sought to develop a new series of ABMs that can be readily functionalized with imaging/

Received: April 9, 2019
Revised: May 9, 2019
Published: May 13, 2019

DOI: 10.1021/acs.bioconjchem.9b00258
Bioconjugate Chem. 2019, 30, 1711−1723

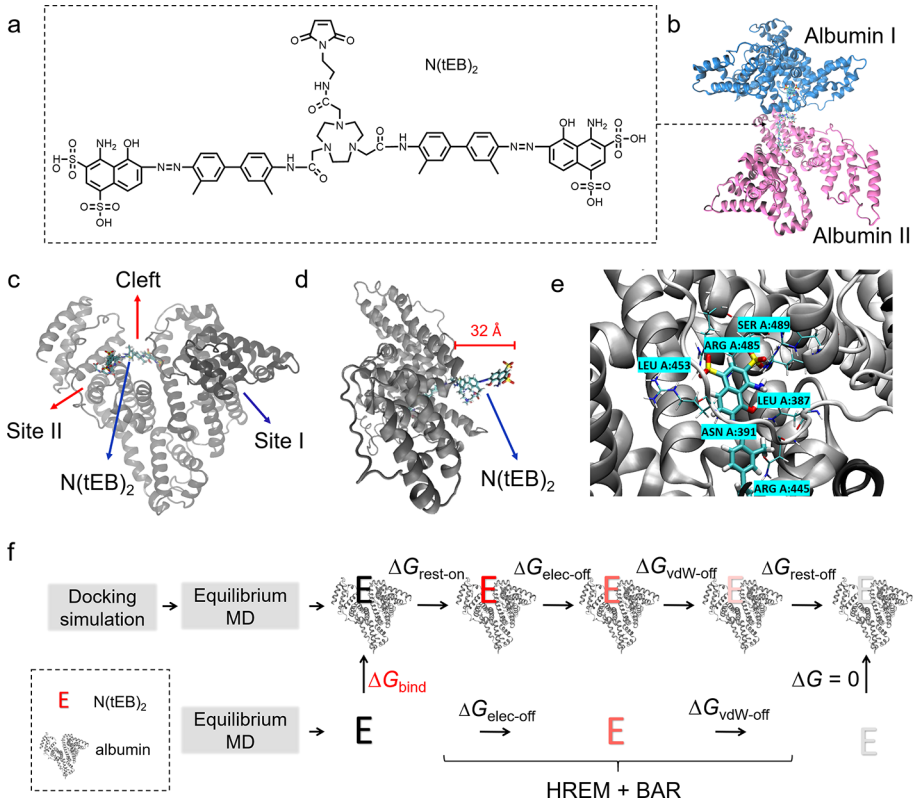

Figure 1. Modeling simulation for $N(tEB)_2$ and human serum albumin (HSA, DIB: 1E78) molecules. (a) Chemical structure of $N(tEB)_2$. (b) 3D figure of the albumin-$N(tEB)_2$-albumin dimer, with an inserted $N(tEB)_2$ in the center of two albumins. (c) Front projection of the most preferable binding site for $N(tEB)_2$ and HSA through simulated docking poses of the most preferable binding site for $N(tEB)_2$ and HSA. (d) Side projection of the binding pose for $N(tEB)_2$ and HSA, showing one inserted head and the other head available for albumin binding. (e) Detailed docking poses and interaction for $N(tEB)_2$ and HSA. (f) Docking simulation combined with thermodynamic cycle in the double decoupling method. The binding poses of the host−guest complex, albumin(s)-$N(tEB)_2$ in this case, were determined by the docking method. Then the conformations of the free guest molecule (E) and the host−guest complex (A) were prepared using classical molecular dynamics (MD) simulations. A restraint was imposed on the guest−host complex to prevent the guest molecule from leaving the binding pocket. The free energy for turning on this restraint ($\Delta G_{rest\text{-}on}$) was computed by using a thermodynamic integral (TI) approach. Next, the nonbonded interaction free energies, including the electrostatic component (ΔG_{elec}) and the van der Waals (vdW) component (ΔG_{vdW}), for both free guest molecule and host−guest complex were computed by using a Hamiltonian replica exchange method followed by the Bennett acceptance ratio (BAR) analysis. Finally, the imposed restraint was turned off and the corresponding free energy ($\Delta G_{rest\text{-}off}$) was computed by eq 1 in this work. When the nonbonded interaction free energies for both free guest molecule and host−guest complex were completely turned off without any restraint, the free energy change between these two systems was set to be zero since there was no coupling between them. With the help of this thermodynamic cycle, the binding free energy was defined as $\Delta G_{bind} = \Delta G_{elec}(E) + \Delta G_{vdW}(E) - \Delta G_{elec}(A) - \Delta G_{vdW}(A) - \Delta G_{rest\text{-}on} - \Delta G_{rest\text{-}off} + \Delta P\Delta V$, where the last term is the work to account for the pressure and volume change between the two systems.

therapeutic molecules, while retaining the high binding affinity of the parental EB dye.

Considering the enhanced functional affinity in biological processes, multivalency is an effective strategy to increase the interaction of individual ligands with their respective receptors.[28−31] We thus constructed a virtual library of tEB dimers ($(tEB)_2$) with different linkers (Figures 1 and 2) and screened the library based on computational modeling. With two albumin binding motifs (4-amimo-5-hydroxynaphthalene-1,3-disulfonic acids), $(tEB)_2$ is expected to bind two albumin molecules and form a reversible albumin-$(tEB)_2$-albumin sandwich structure (Figure 1a,b). The 1,4,7-triazacyclononane-1,4,7-trisacetic acid (NOTA) group was introduced to enable radiolabeling and imaging. We hypothesize that this in vivo dimerization will result in enhanced tumor retention after intravenous injection compared with previous EB constructs with only one binding moiety. Furthermore, this albumin-dimer will create a cavity whereby a conjugated therapeutic small molecule can be protected from enzymatic degradation.

RESULTS

Evans Blue and EB Derivatives Bind to Cleft and Site II on Albumin. We computationally modeled the binding sites for the albumin binding motifs, using AutoDock Vina software package to generate the docking poses. The center cleft on albumin was found to be the most preferable binding site, followed by site II (Figure 1c-e and SI Videos 1 and 2). Our results ran contrary to previously published literature stating that EB binds preferentially to site I.[32,33] To substantiate this finding, we incubated the recombinant HSA subunits (three separate domains of albumin) with EB and performed high-resolution liquid chromatography−mass spectrometry (LC-MS) to detect complex formation between the individual recombinant HSA subunits with EB. Only the domain III subunit, which contains site II, was observed to complex with EB by LC-MS (Figure S3). Collectively, these data indicated the unexplored cleft and/or site II on domain III rather than site I on domain II A was the binding site(s) for EB and its derivatives.

DOI: 10.1021/acs.bioconjchem.9b00258
Bioconjugate Chem. 2019, 30, 1711−1723

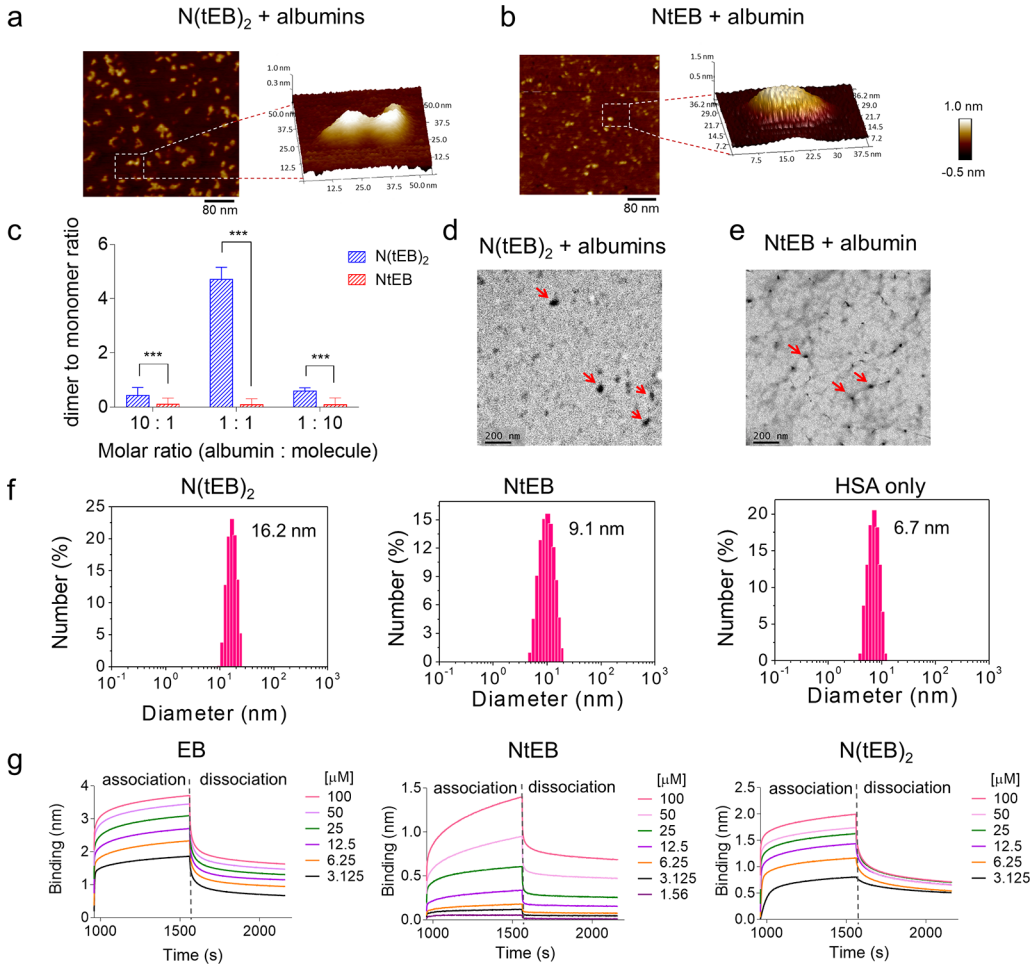

Figure 2. Characterization of the interaction between $N(tEB)_2$ and albumin: (a) Atomic Force Microscope (AFM) images showing in vitro albumin-$N(tEB)_2$-albumin dimer. (b) AFM images showing in vitro NtEB-albumin monomers. (c) Quantification of mixture of the $N(tEB)_2$ and NtEB with HSA by molar ratio of 1:1, 10:1, and 1:10, respectively. The "dimer" (length: >25 nm, dumbbell-shaped) and "monomer" (length: ≤25 nm, no dumbbell-shaped morphology) were defined by ImageJ. TEM imaging described the size of (d) $N(tEB)_2$-albumins complex of 17.1 ± 3.2 nm and that of (e) NtEB-albumin mixture of 9.3 ± 0.6 nm, revealing that the dimerization was induced by $N(tEB)_2$. (f) Dynamic Light Scattering (DLS) analysis showing the diameter of $N(tEB)_2$ and NtEB complex when mixed with albumin and the free albumin solution. (g) Binding affinity of HSA for EB, NtEB, and $N(tEB)_2$ analyzed by the Biolayer Interference method.

Design and Optimization of $N(tEB)_2$ with Modeling Simulation. After confirming the binding sites of EB in albumin, we designed a library of derivatives with two albumin binding motifs and linkers with variable lengths, ranging from 5.2 to 10.8 Å (SI Table S1). Docking simulation and protein−protein interaction analysis were conducted to screen for optimal binders. A prospective structure $(tEB)_2$ was first constructed, with either an aliphatic chain or a NOTA group in the center (Figures 1 and 2). The $(tEB)_2$ with only an aliphatic chain as the linker was extremely flexible and tended to fold, so it was unable to cross-link two albumin molecules (Figures S1a-c and 4). A thiourea group was introduced to promote intramolecular hydrogen bond formation with the NOTA group, and to stabilize the rigid conformation of $(tEB)_2$ molecule (Figures S1d and 5a). Next, we screened the rigid-confirmation scaffolds listed in Figures S1d and 2a, with different aliphatic chain lengths ($1 \leq n \leq 8$) (SI Table S1) to determine the optimal distance for albumin binding (SI Table S2 and Figure S6). We evaluated the albumin interaction through the molecular mechanics/Poisson−Boltzmann surface area (MM/PBSA) analysis on five 1 ns conformation sampling trajectories of the proteins with distances of 60/70/80/90/100 Å between their centers of mass. The distance range of 64−80 Å (minimum distance of 4.7−16.4 Å from edge to edge) was found to be the best for increasing albumin−albumin intermolecular attraction and avoiding steric hindrance between the two adjacent albumin molecules, indicating that the scaffolds with an aliphatic chain consisting of 3 to 5 methylene groups were optimal for dual albumin binding. Alternatively, when the NOTA group was engineered as part of the backbone rather than a side-chain moiety on the aliphatic chain, we also observed restricted self-folding of $(tEB)_2$ (Figures S2 and 5b).

When $N(tEB)_2$ and EB were placed in a cubic TIP3P water model with a buffer space 12 Å on each side using both the parallel and angular starting poses, the free EB dye showed a strong tendency to form $\pi-\pi$ stacking. $N(tEB)_2$ avoided intermolecular stacking and self-assembly (Figure S7). The results from absolute binding free energy calculations between the $N(tEB)_2$ and albumin(s) via a double-decoupling scheme (Figure 1f and SI Table S3) confirmed that the most stable complex for the mixture of $N(tEB)_2$ and albumin molecules was the "sandwich" HSA-$N(tEB)_2$-HSA dimer with ΔG_{bind} of −22.3 kcal/mol), which was far less than that of $N(tEB)_2$-HSA

DOI: 10.1021/acs.bioconjchem.9b00258
Bioconjugate Chem. 2019, 30, 1711−1723

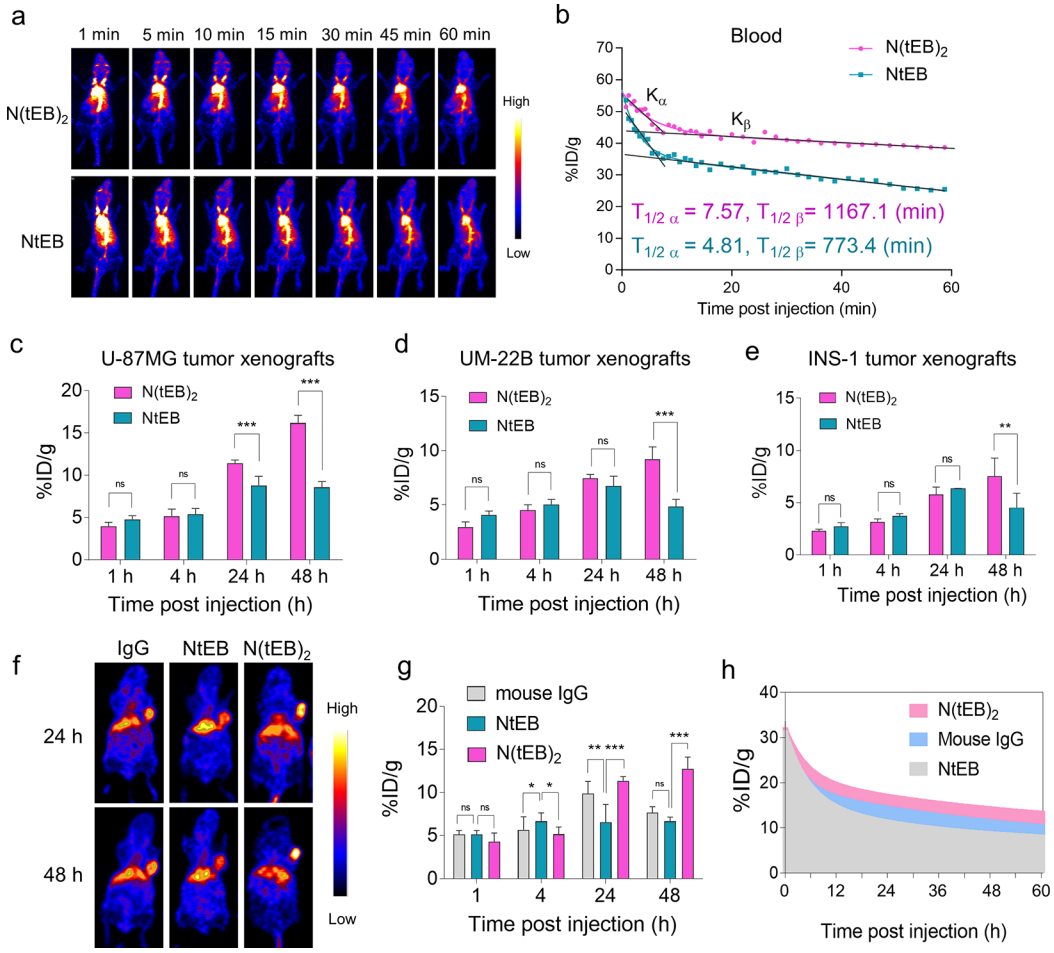

Figure 3. In vivo cross-link $N(tEB)_2$-albumins dimer improved pharmacokinetics and tumor targeting ability. (a) Comparison of kinetic PET imaging for mice with ^{18}F labeled $N(tEB)_2$ and NtEB administrated in healthy mice at various time points, respectively. (b) Comparison of the half-life of the ^{18}F labeled $N(tEB)_2$ and NtEB through two-phase linear regression of the time activity curves over heart at various time points, respectively. Quantification of tumor uptake of ^{64}Cu labeled $N(tEB)_2$ and NtEB in (c) U-87MG, (d) UM-22B, and (e) INS-1 tumor xenografts at 1, 4, 24, and 48 h p.i., respectively. (f) PET images of ^{64}Cu labeled mouse IgG, NtEB, and $N(tEB)_2$. (g) Comparison of the tumor uptake of ^{64}Cu labeled mouse IgG, NtEB, and $N(tEB)_2$ in U-87MG tumor xenografts at different time points p.i., respectively. (h) Comparison of time activity curves (TAC) over heart for ^{64}Cu labeled IgG, NtEB, and $N(tEB)_2$, respectively.

monomer (ΔG_{bind} = −7.1 kcal/mol) (SI Table S4). The data suggests that this optimized configuration allows for binding cooperativity and overcomes steric hindrance for cross-linking two albumins.

$N(tEB)_2$ Cross-Links Albumin to Form Dimers in Vitro. We identified and synthesized two $N(tEB)_2$ ($N(tEB)_2$ 1 and $N(tEB)_2$ 2) following the synthesis schemes in SI Figures 8–11. The modeling also revealed that one $N(tEB)_2$ was able to attach two albumin molecules to form HSA-$N(tEB)_2$-HSA dimer. We performed atomic force microscopy (AFM) to study the morphological structures of the complex. Both $N(tEB)_2$ and a control molecule NtEB were incubated with HSA at molar ratio of 1:1, 10:1, and 1:10, respectively. Dimerization of albumin mediated by $N(tEB)_2$ was observed at all tested molar ratios, while no apparent albumin dimers were identified in the mixture of NtEB and HSA (Figure 2a-c). These results were further substantiated by transmission electron microscopy (TEM), dynamic light scattering (DLS) and high-resolution LC-MS. The size of $N(tEB)_2$-albumins dimer determined by TEM was significantly larger than that of NtEB-albumin monomer (17.1 ± 3.2 vs 9.3 ± 0.6 nm). The hydrodynamic diameters detected by DLS were 6.7, 9.1, and 16.2 nm for free albumin, NtEB-albumin, and $N(tEB)_2$-albumins, respectively (Figure 2d-f and Figure S12). Furthermore, with samples containing both albumin and $N(tEB)_2$, peak clusters with double the molecular weights were identified with high-resolution LC-MS, indicating the existence of albumin dimers (Figure S13).

The binding affinity of the optimized $N(tEB)_2$ with albumin was determined by using biolayer interference (BLI). The K_d value of $N(tEB)_2$ is 1.8 μM, which was 43 times lower than that for NtEB (K_d = 79 μM) and 2 times lower than that for EB (K_d = 3.7 μM) (SI Table S5). The $N(tEB)_2$ additionally showed relatively high K_{on} value (4.71×10^4 M^{-1} s^{-1}), and low k_{off} value (0.10 s^{-1}), compared to EB and NtEB (Figure 2g and SI Table S5). The quick association and slow dissociation with albumin further governed the favorable binding capacity of $N(tEB)_2$.

$N(tEB)_2$ Shows Improved Pharmacokinetics and Enhanced Tumor Accumulation. It is expected that increased binding affinity and in vivo cross-linking of albumin will result in extended circulation time of $N(tEB)_2$. Hence, the in vivo dynamic positron emission tomography (PET) was performed in healthy mice to determine the pharmacokinetics

DOI: 10.1021/acs.bioconjchem.9b00258
Bioconjugate Chem. 2019, 30, 1711−1723

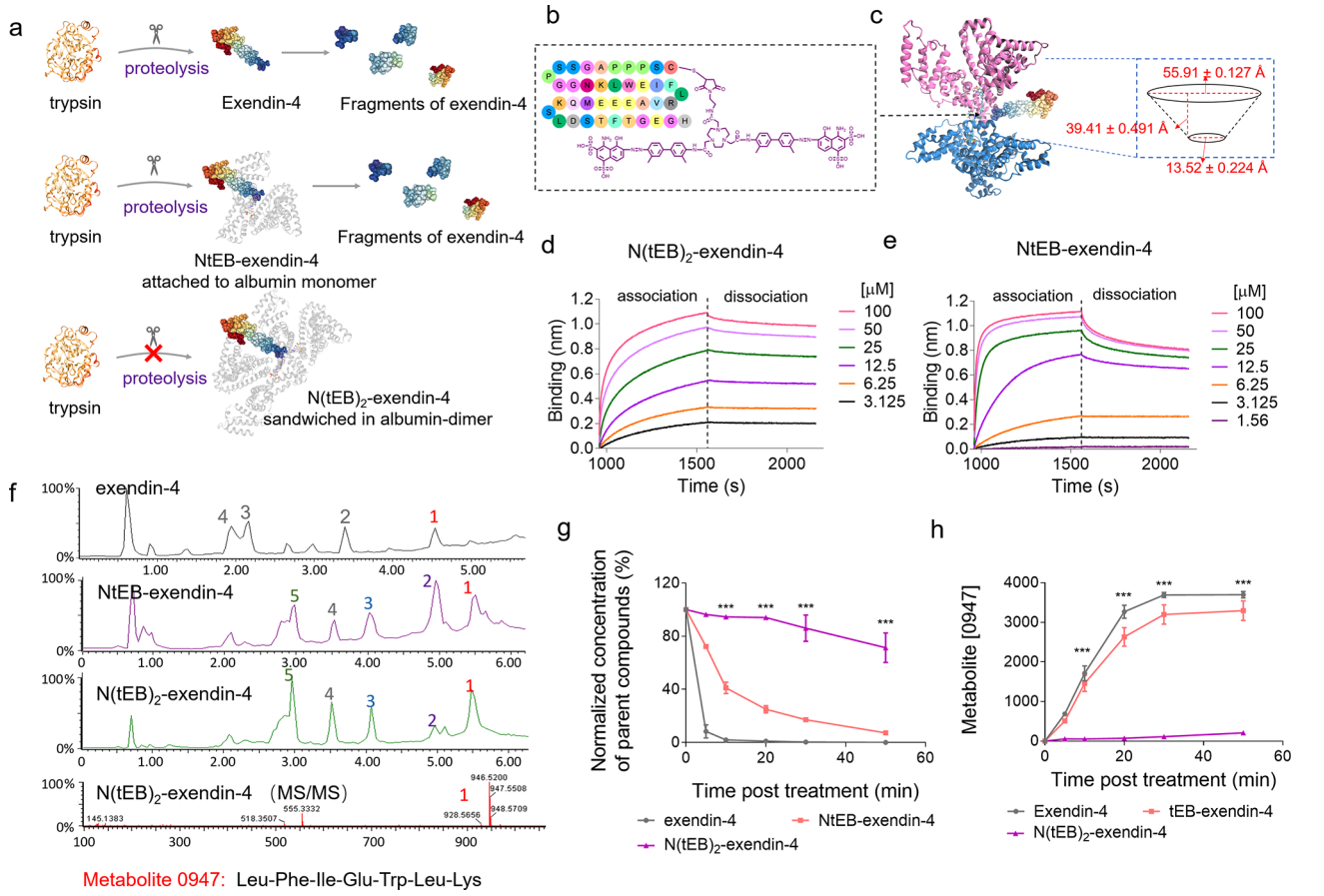

Figure 4. $N(tEB)_2$ albumin dimer protects metabolically labile drug from degradation. (a) Schematic of the mechanism of resistance to proteolysis through sandwiching in albumins. The free exendin-4 was easily digested by trypsin into small fragments. By tagging to an albumin molecule, the NtEB-exendin-4 is also exposed to the enzyme and liable to further digestion. In sharp contrast, being sandwiched into an albumin dimer, the $N(tEB)_2$-exendin-4 is protected from proteolysis. (b) Close-up view of the structure of $N(tEB)_2$ and the sequence of the attached peptide, exendin-4. (c) Modeling of albumins dimer showing a sufficient space to sandwich the $N(tEB)_2$ conjugated small peptide. Binding affinities for (d) NtEB-exendin-4 and (e) $N(tEB)_2$-exendin-4 with albumin analyzed by BLI. The dashed lines separate the association and the dissociation phases. (f) Representative LC-MS characterization (the upper three figures) showed four/five major fragment peaks (labeled with Arabic numerals) after digestion of exendin-4, NtEB-exendin-4, and $N(tEB)_2$-exendin-4 with trypsin at 40 min post digestion, respectively. The metabolite, Leu-Phe-Ile-Glu-Trp-Leu-Lys (MS: 0947) in the lower MS/MS figure, was observed for all three samples. Hence, this metabolite was tracked to compare the antiproteolysis effect of these three compounds in the presence of HSA. (g) LC-MS analysis showing the percentage of the parent compounds ($N(tEB)_2$-exendin-4, NtEB-exendin-4, and free exendin-4) remaining after 0, 5, 10, 20, 30, and 50 min incubation with serum albumin in the presence of trypsin. Error bars represent the mean ± s.t.d. of three replicates. (h) Metabolite analysis for exedin-4, NtEB-exendin-4, and $N(tEB)_2$-exendin-4 treated by trypsin in the presence of HSA.

of ^{18}F labeled $N(tEB)_2$ or NtEB (Figure 3a). After intravenous administration, both ^{18}F-$N(tEB)_2$ and ^{18}F-NtEB showed high radioactivity accumulation and retention in the circulatory system, with clear delineation of highly perfused organs including heart, liver, kidneys, and spleen. Regions of interest (ROIs) were drawn over different organs to generate time–activity curves (TACs). Based on the TACs, linear regression was used to estimate the dominant half-life and clearance of these two tracers. As expected, ^{18}F–$N(tEB)_2$ showed 1.66 times slower clearance from circulation in vivo than ^{18}F-NtEB (Figure 3b and Figure S14), indicating the potential of ^{18}F–$N(tEB)_2$ to be used as a blood pool imaging agent.

Due to the aberrant and leaky vasculature within tumor tissues, drug delivery based on the enhanced permeability and retention (EPR) effect has been a well-established strategy. Long circulation half-life is the prerequisite for EPR-based drug delivery. Tumor retention of $N(tEB)_2$ was assessed with PET imaging in three tumor models with different levels of blood supply and vascular permeability, after labeling with ^{64}Cu ($t_{1/2}$ = 12.6 h) (Figure 3c-e). Compared with NtEB, the tumor uptake of $N(tEB)_2$ was significantly improved in all tested tumor models at late time points (24 and/or 48 h post-injection (p.i.)), despite UM-22B and INS-1 exhibiting a relative slower maximal accumulation than U-87MG (Figure 3c-e and Figure S15a). Meanwhile, the clearance of ^{64}Cu-$N(tEB)_2$ was slower than the ^{64}Cu-NtEB in the blood pool, which contributes to the higher retention in tumor (Figure S15b). The high retention of $N(tEB)_2$ in tumor sites was further corroborated with the ex vivo biodistributions study at 48 h p.i. (Figure S16).

The overall size of $N(tEB)_2$ cross-linked albumin dimer is more than 130 kDa, which is similar to immunoglobulin G (IgG) in regard to molecular weight and hydrodynamic diameter. PET imaging revealed comparable tumor retention of $N(tEB)_2$ and IgG at 24 h p.i. However, the tumor retention of $N(tEB)_2$ was significantly higher than that of IgG at 48 h p.i., indicating the former is more efficient for EPR mediated tumor delivery (Figure 3f-h).

DOI: 10.1021/acs.bioconjchem.9b00258
Bioconjugate Chem. 2019, 30, 1711–1723

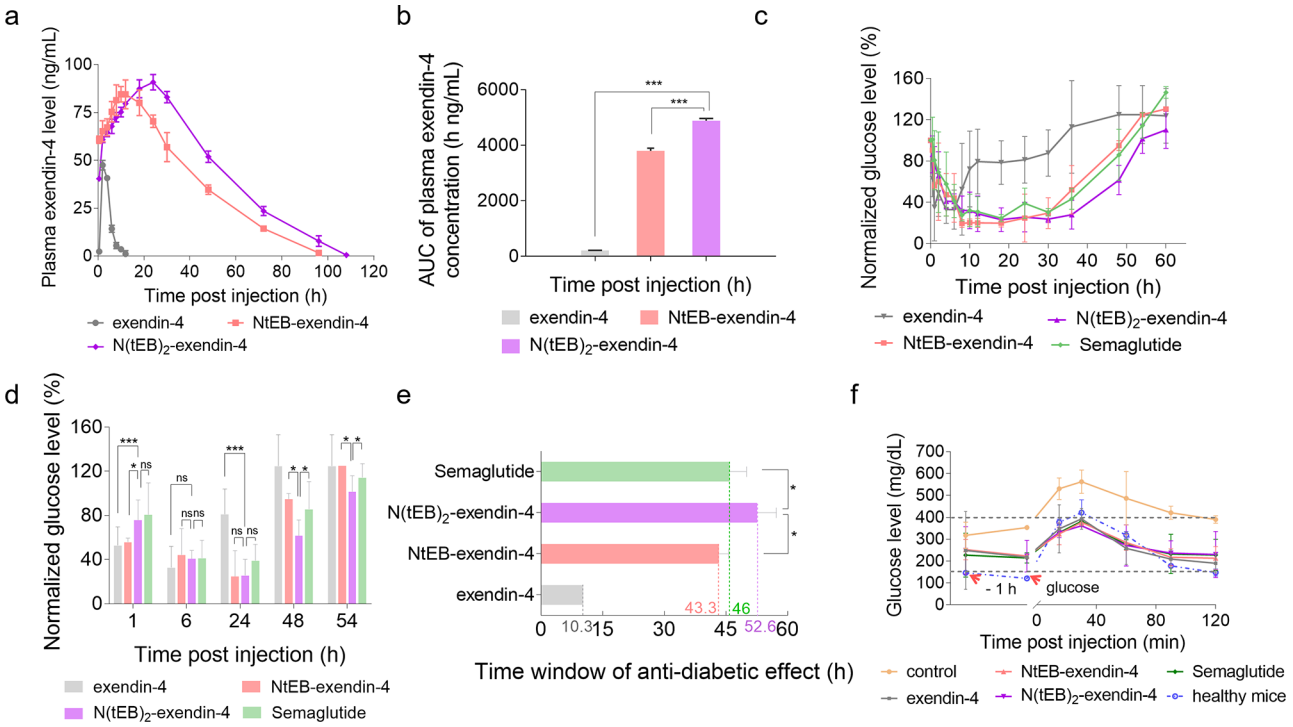

Figure 5. N(tEB)$_2$-exendin-4 afforded the long-acting drug release and therapeutic efficacy in type 2 diabetes mellitus (T2DM) mice. (a) Plasma concentration of exendin-4 after administering an equivalent dose of exendin-4 in both the NtEB-exendin-4 and N(tEB)$_2$-exendin-4 compounds as well as free exendin-4 (n = 3 per group). Error bars represent the mean ± st.d. of three biological replicates. (b) Area Under the Curve (AUC) of plasma exendin-4 concentration up to 120 h. Error bars represent the mean ± st.d. (c-d) Long-term blood glucose monitoring in T2DM after treatment of exendin-4, NtEB-exendin-4, N(tEB)$_2$-exendin-4, as well as semaglutide, respectively (3 T2DM in each group). (e) Time window from the 50% reduction of the glucose level to rebound to the original level. Error bars represent the mean ± st.d. of three replicates. (f) IPGTT of diabetic mice at 2 h post-administration of exendin-4, EB-exendin-4, N(tEB)$_2$-exendin-4, or semaglutide (3 healthy mice or 3 T2DM in each group). Error bars represent the mean ± st.d. p values of <0.05 were considered statistically significant. (***p < 0.001, *p < 0.05, ns: not significant (p > 0.05).)

N(tEB)$_2$ Protects Drug from Enzymatic Degradation. When a peptide being attached to N(tEB)$_2$ through a facile thiol-maleimide reaction and sandwiched between two albumins, it will be protected from enzymatic degradation while it is in complex with albumin dimers via N(tEB)$_2$ (Figure 4a).

To test the hypothesis, exendin-4 peptide, a glucagon-like peptide-1 (GLP-1) agonist, was linked to N(tEB)$_2$ and NtEB to provide two conjugates, N(tEB)$_2$-exendin-4 and NtEB-exendin-4, respectively (Figure 4b,c and Figure S17−18). N(tEB)$_2$-exendin-4 showed significant higher binding affinity with albumin than NtEB-exendin-4 (K_d ~ 0.68 μM vs 1.4 μM), with relatively fast association and slow dissociation (Figure 4d,e; SI Table S6). A trypsin digestion study was adopted to further investigate the peptide protection role of N(tEB)$_2$-albumins complex (Figure 4f). The exendin-4 peptide contains one arginine and two lysine residues which are cleavage sites for trypsin. When exendin-4 was subjected to trypsin digestion, four main fragments were observed using LC-MS post various incubation times as expected, demonstrating a convincing evaluation strategy for antidegradation effect (Figures S19 and 20). Remarkably, N(tEB)$_2$-exendin-4 showed highest resistance to trypsin degradation with the presence of albumin, with ~70% of intact form after incubating with trypsin for 50 min, which is significantly higher than that of N(tEB) exendin-4 (~10%, P < 0.001) and exendin-4 (<0.1%, P < 0.001) (Figure 4g). From the four major fragments of exendin-4, we chose one fragment commonly shared by N(tEB)$_2$-exendin-4, NtEB-exendin-4, and exendin-4 for further quantification. Consistently, the fragments generated from N(tEB)$_2$-exendin-4 increased much more slowly than that from NtEB-exendin-4 and exendin-4, further confirming the peptide protection effect of N(tEB)$_2$ through sandwiching the peptide by albumin proteins (Figure 4h and Figures S21−23).

N(tEB)$_2$-Exendin-4 Shows Enhanced Antidiabetic Efficacy. Based on the structure of N(tEB)$_2$ cross-linked albumins dimer and its favorable in vivo behavior, it is rational to hypothesize that a peptide conjugated to N(tEB)$_2$ will be endowed with extended circulation half-life. Consequently, enhanced therapeutic efficacy will be achieved.

For evaluation of pharmacokinetics, the concentration of exendin-4 was measured using ELISA in venous blood samples acquired at multiple time points post subcutaneous injection. Exendin-4 alone showed fast entry into circulation from injection site, and cleared from the body within 12 h p.i. Compared with free exendin-4, NtEB-exendin-4 showed a dramatic increase in circulation time with the peak concentration observed at 12 h p.i., and clearance by 96 h p.i. Remarkably, N(tEB)$_2$-exendin-4 enabled a significantly prolonged release of exendin-4 with peak concentration of exendin-4 at up to unprecedented 24 h p.i., and retention time up to 108 h p.i. (Figure 5a,b).

The hypoglycemic properties of free exendin-4, NtEB-exendin-4, and N(tEB)$_2$-exendin-4 were next tested in type 2 diabetes mellitus (T2DM) mice after subcutaneous injection. Semaglutide, a long-acting GLP-1 agonist which recently

DOI: 10.1021/acs.bioconjchem.9b00258
Bioconjugate Chem. 2019, 30, 1711−1723

received FDA approval and arguably the best commercial weekly formula so far, was used as the positive control. The glucose levels of the four treated cohorts were monitored at different time points post administration (Figure S24). After baseline plasma glucose concentration normalization, it was observed that glucose level was reduced by approximately 50% at 1 h p.i. of free exendin-4 and NtEB-exendin-4, and by approximately 20% at 1 h p.i. of $N(tEB)_2$-exendin-4 and semaglutide. This was attributed to the delayed release and enhanced residence time of $N(tEB)_2$-exendin-4 and semaglutide (Figure 5c,d). The glucose recovery time of NtEB-exendin-4 (515.00 ± 25.0 mg/dL at 48 h), semaglutide (475.33 ± 55.4 mg/dL at 54 h), and $N(tEB)_2$-exendin-4 (519 ± 5.35 mg/dL at 54 h) treated mice were much longer than free exendin-4 (389.67 ± 44.3 mg/dL at 12 h) (Figure S24b,c). The effective time window of $N(tEB)_2$-exendin-4 (52.6 h), which is defined as the time duration from 50% reduction of glucose level to the rebound to the original level, was significantly longer than the three other treatment groups (Semaglutide: 46 h, NtEB-exendin-4:43.3 h, and exendin-4:10.3 h) (Figure 5e). Overall, these data demonstrated that $N(tEB)_2$-exendin-4 was superior to free exendin-4, and NtEB-exendin 4 in sustaining a hypoglycemic effect, and comparable or even greater hypoglycemic potency than FDA-approved semaglutide. In addition, the intraperitoneal glucose tolerance test (IPGTT) confirmed the efficacy of glycemic control with $N(tEB)_2$-exendin-4, suggesting effective responsiveness (Figure 5f).

DISCUSSION

Albumin is a versatile carrier for many endogenous and exogenous small molecules.[32] So far, two high affinity binding sites for small heterocyclic or aromatic compounds have been identified including binding site I on subdomain IIA and site II on subdomain IIIA.[34] Although it has been speculated that EB binds to the site I of albumin,[32,33] to our knowledge, all of the publications cited the study published by Freedman and Johnson in 1969.[32,33,35] Freedman and Johnson computed the equilibrium constants and rate binding constants for the EB-albumin system. Both the equilibrium and kinetic data they obtained can be classified into two groups, by which they realized that there are two types of independent binding sites on albumin for EB. However, no experimental data was provided to identify the EB binding site on albumin. Hence, the assignment of EB to site I was never truly verified. We propose that, for the first time, the unexploited cleft and site II of serum albumin are likely the binding sites for EB and its derivatives based on predictive docking and high-resolution LC-MS data. The computational docking was performed by AutoDock Vina, an academic docking program with high speed and accuracy,[36] as well as the best scoring powers among ten famous docking programs.[37] Therefore, it has been broadly applied to predict the binding poses for biomacromolecule−ligand complexes to explore the underlying mechanism.[38,39] This finding reveals the binding interaction between EB derivatives and albumin, and possibly serves as a guide for the synthesis of next generation high-performance albumin binders.

The approach of in vivo dimerization of two albumins to form a sandwich structure is attractive for multiple reasons. First, by multivalence effect, $N(tEB)_2$ offers an increased chance to attach albumin, resulting in increased binding affinity to albumin and decreased free $N(tEB)_2$ molecules diffusing from the blood vessel and interstitial fluid to the regional tissues relative to NtEB. This provides an entirely new interaction strategy for improving either the blood pool/vessel imaging or lymphatic vessel imaging with enhanced signal to background ratio. With a K_d value of 1.8 μM, it may not be appropriate to claim that $N(tEB)_2$ binds to albumin with high affinity, compared with other ABMs with K_d values in the nM range.[13] However, the high abundance of albumin in serum or interstitial fluid can easily facilitate complex formation. Moreover, reversible complexation is advantageous for drug release and to ensure that the intrinsic activity of the conjugate is maintained.[40] The equilibrium between the ABM and albumin therefore is crucial for improving the pharmacokinetics. In our study, the $N(tEB)_2$ reversibly binds to albumins with relatively high affinity and prolonged circulation time in vivo, enabling high clinical potential as a smart delivery platform for enhanced imaging agents and long-acting therapeutics.

Second, the biomimetic albumins cross-linking, bridged by the aqueous soluble $N(tEB)_2$, displays predominant advantages on in vivo assembling with desired nanoscale, which provides a higher accumulation in the tumor region compared to NtEB-albumin monomer and biomimetic drug carriers with high biocompatibility.[41] The in vivo cross-linking $N(tEB)_2$-albumins dimer increased the tumor retention compared to the NtEB-albumin monomer at late time points, probably due to both the EPR effect and extended circulation time. We previously performed radiotherapy for neuroendocrine tumor bearing mice using radionuclide labeled EB derivative conjugated with a targeting peptide, octreotate, which revealed a superior imaging capacity (tumor uptake of ~75%ID/g in AR42J tumor xenografts) and an unprecedented therapeutic efficacy (response rate of 100% in AR42J tumor model).[24] We have collected conclusive data here establishing the superior clinical potential of $N(tEB)_2$ compared with standard EB or previous NtEB derivatives. Hence, this newly developed diagnostic imaging derivative could undoubtedly be used as a more effective drug/radionuclide isotope for tumor therapy.

Last but most important, the $N(tEB)_2$ conjugated peptides can be imbedded in between the albumin dimer, and thus, this albumin dimer provides a cavity to protect the peptides from being degraded by enzymes during circulation. The protection of peptides from serum proteases has been reported with a binding tag to transthyretin (TTR) in serum.[40] However, the amount of TTR in blood (0.25−0.30 g/L vs 35−50 g/L) is much lower than that of 390 albumin, and its half-life (48 hours vs 19 days) is much shorter too. In this study, the enzymatic protection of $N(tEB)_2$ of exendin-4 against trypsin was confirmed with LC-MS evaluation in the presence of albumin. We believe that this important feature of $N(tEB)_2$ can be extrapolated to other peptide-based drugs, especially those that are protease-sensitive. More importantly, our $N(tEB)_2$-exendin-4 bioconjugate confirmed this revolutionized design with expected long-acting hypoglycemic effect in type 2 diabetes mellitus (T2DM). The hypoglycemic effect of $N(tEB)_2$-exendin-4 was superior to both previously tested NtEB-exendin-4 (Abextide) and the newly FDA approved semaglutide.[42,43] Therefore, we speculated that the improved hypoglycemic effect of $N(tEB)_2$-exendin-4 was primarily due to increased residence time and extended circulating half-life. Although not explicitly addressed in this study, we envision that our approach can be potentially applicable for extending

DOI: 10.1021/acs.bioconjchem.9b00258
Bioconjugate Chem. 2019, 30, 1711−1723

the half-lives of oligonucleotides, lipids, polysaccharides, and other small molecule drugs, in addition to peptides.

In conclusion, we developed a new class of ABMs with several promising biomedical applications. Depending on the route of administration, by dimerization of two molecules of albumin in situ, $N(tEB)_2$ showed increased binding ability with albumin and therefore sustained local residence after subcutaneous administration and extended circulating half-life after intravenous injection. $N(tEB)_2$ also display an inherent propensity to accumulate in tumor tissues because of the EPR effect, offering a potential application for tumor-targeted drugs/radionuclides therapy. With simple thiol-maleimide chemistry, $N(tEB)_2$ can be derivatized for long-acting drug delivery. More importantly, by partitioning the drug of interest between two albumins it protects the drug against enzymatic degradation during circulation. This potentially opens the door for combining ABMs with metabolically labile compounds. Collectively, these properties support $N(tEB)_2$ as a versatile platform for the development of next-stage long-lasting therapeutics.

METHODS

Double-Decoupling Scheme. The binding affinity can be computed using double-decoupling scheme (Figure 1a)[44,45] which allows one to calculate the absolute binding free energy at a given conformation. It is necessary to prevent the guest from being far away from the host when guest−host interactions become very weak to obtain well-converged results with this scheme. As indicated from the thermodynamic cycle of the double-decoupling scheme, the absolute binding free energy of a complex is equivalent to the difference between the decoupling free energy of a ligand in the bound state and the solvation free of a ligand in the monomeric state[46]

$$\Delta G_{\text{bind}} = \Delta G^{\text{C}}_{\text{rest-on}} - \Delta G^{\text{C}}_{\text{elec}} - \Delta G^{\text{C}}_{\text{vdW}} - \Delta G^{\text{C}}_{\text{rest-off}} + \Delta G^{\text{M}}_{\text{elec}} + \Delta G^{\text{M}}_{\text{vdW}} \quad (1)$$

where $\Delta G^{\text{C}}_{\text{rest-on}}$ and $\Delta G^{\text{C}}_{\text{rest-off}}$ are the free energies for turning on/off restraints, $\Delta G^{\text{C}}_{\text{elec}}$ and $\Delta G^{\text{M}}_{\text{elec}}$ are the free energies of decoupling electrostatic interactions of the guest molecule in the bound state and the monomeric state, respectively, and $\Delta G^{\text{C}}_{\text{vdW}}$ and $\Delta G^{\text{M}}_{\text{vdW}}$ are those for the vdW interactions. The free energy of removing restraints $\Delta G^{\text{C}}_{\text{rest-off}}$ is calculated by the following formula[45]

$$\Delta G^{\text{C}}_{\text{rest-off}} = -kT \ln \frac{8\pi^2 V (K_r K_{\theta_A} K_{\theta_B} K_{\phi_A} K_{\phi_B} K_{\phi_C})^{1/2}}{r_0^2 \sin\theta_{A,0} \sin\theta_{B,0} (2\pi kT)^3} \quad (2)$$

where V is the volume for the unit cell, r_0 is the reference distance of a distance restraint, θ_A and θ_B are reference angles of angle restraints, and K values are the force constants of the six restraints.

Thermodynamic Integration (TI). TI method[47,48] calculates the free energy difference between two states 0 and 1 by using the derivatives of the potential energy with respect to a state variable λ, $\frac{\partial U(x,\lambda)}{\partial \lambda}$. Using integration, the free energy difference between state 0 and 1 is

$$\Delta G^{\text{TI}} = \int_0^1 \left(\frac{\partial U(x,\lambda)}{\partial \lambda} \right)_\lambda \text{d}\lambda \quad (3)$$

Hamiltonian replica exchange method (HREM) A HREM[49,50] simulation uses multiple replicas to sample a phase space simultaneously, while replicas are swapped periodically.[49] Each replica corresponds to a different environmental condition. It is well-known that proper exchanges between Hamiltonians enhance sampling efficiency while preserving the Boltzmann distribution.[50,51] In HREM, the ratio between the probability of exchanging x in the mth replica and y in nth replica $W(x,E_m;y,E_n)$ and that of the reverse process $W(y,E_m;x,E_n)$ must follow the relation

$$\frac{W(x, E_m; y, E_n)}{W(y, E_m; x, E_n)} = \text{e}^{-\beta\Delta} \quad (4)$$

where

$$\Delta = E_m(y) - E_m(x) + E_n(x) - E_n(y) \quad (5)$$

and this condition can be satisfied if the Metropolis-type criterion is used for exchanges,

$$W(x, E_m; y, E_n) = \begin{cases} \text{e}^{-\beta\Delta}, \text{ if } \Delta > 0 \\ 1, \text{ otherwise} \end{cases} \quad (6)$$

Bennett's Acceptance Ratio (BAR). BAR method[52,53] was utilized for post processing, which uses information from a pair of simulations. From the ensembles sampled with two simulations, the free energy difference is calculated according to

$$\Delta G^{\text{BAR}} = -\frac{1}{\beta} \ln \frac{\langle f(U_0 - U_1 + C) \rangle_1}{\langle f(U_1 - U_0 - C) \rangle_0} + C \quad (7)$$

where f is the Fermi function and C is a constant that is solved by an iterative procedure.[54]

Computational Details. For the host, i.e., the Human Serum Albumin protein, all residues in the X-ray structure (PDB code 1E78)[55] were kept except for S−S bond patching and hydrogens, which were built using CHARMM software.[56] AutoDock Vina,[57] as one of the most popular docking softwares, was used for the predocking process to generate the initial poses. For this special case, only one wing of the ligand ($N(tEB)_2$) is docked with the host molecule (Albumin). After docking, all the simulations were performed with CHARMM 41b1. The force field parameters of $N(tEB)_2$ were generated with the CGenFF server.[58,59] The complex structure was then solvated in a cubic TIP3P water box with a buffer space of 12 Å on each side. HREM simulation was performed after 1 ns NPT equilibrium to calculate the free energy contributions of the electrostatic and vdW interactions. Due to the high flexibility of the guest molecule, $N(tEB)_2$, 100 replicas (see Supporting Information for more details) are necessary for the HREM simulation in both bound and monomeric states. All the procedures are summarized in Figure 1a.

Synthesis of $N(tEB)_2$ 1. The synthesis procedure is shown in Figure S8. In detail, 4.25 g *o*-tolidine (compound **1**) (4.25 g, 20.0 mmol) and 50 mL dichloromethane were added to a 250 mL glass vial, and then 20 mL di-*tert*-butyl dicarbonate (4.36 g, 20.0 mmol) in dichloromethane was added dropwise to the vial. The mixture was stirred in room temperature (RT) for 24 h, then the solvents were removed under reduced pressure, and the residuum was purified by silicon column to obtain the compound **2**. To 3.12 g of compound **2** in 40 mL water was

DOI: 10.1021/acs.bioconjchem.9b00258
Bioconjugate Chem. 2019, 30, 1711−1723

added 15 mL 2 M HCl; after cooling in an ice bath, 20 mL $NaNO_2$ (2.07 g, 30.0 mmol) was added, the mixture was stirred in ice bath for 20 min, and a yellow diazonium salt solution was formed (compound **3**). $NaHCO_3$ (3.36 g) was added to 3.19 g 1-amino-8-naphthol-2,4-disulfonic acid in 20 mL water, and then compound **3** solutions were added dropwise and the mixture was stirred in an ice bath for 2 h. The solvents were removed under reduced pressure, and the residuum was purified by C18 column to obtain compound **4**. Compound **4** (3.22 g) was added to 20 mL TFA in batches, stirred in RT for 60 min, and then the solvents were removed under reduced pressure, and the residuum was purified by C18 column to obtain the compound **5**. Ammonium hydroxide (1 mL) was added dropwise to 1.08 g compound **5** in DMF, followed by stirring at RT overnight. Then, 0.74 g CS_2 was added to the mixture and stirred at 40 °C for 8 h. The residuum was purified by C18 column to obtain compound **6**. The purified compound **6** (0.58 g) and $Pb(NO_3)_2$ (0.66 g) were mixed in 50 mL acetonitrile overnight at RT. The mixture was purified by HPLC to get compound **7**.

Compound **5** (0.54 g), compound **8** (0.43 g), HATU (0.38 g), and DIPEA (0.26 g) were added to 20 mL DMF, and the mixture was stirred at RT for 24 h. The solvents were removed under reduced pressure, and the residuum was purified by C18 column to obtain compound **9**. To a solution of compound **9** (0.48 g) in 10 mL DMF, 2 mL piperidine was added dropwise in an ice bath, and the mixture was stirred for 2 h at RT. The solvents were removed under reduced pressure, and the residuum was purified by C18 column to obtain the compound **10**. Then, 0.37 g of the compound **10**, 0.25 g NOTA-$(OBut)_2$, 0.19 g HATU, and 0.13 g DIPEA were in turn added to 5 mL DMF. The mixture was stirred at room temperature for 24 h, and then the solvents were removed under reduced pressure. The residuum was purified by C18 column to obtain compound **11**. A solution of compound **11** (0.24 g) in 20 mL TFA was stirred for 2 h at RT, the solvent was removed under reduced pressure, and compound **12** was acquired by C18 column.

Finally, compound **7** (0.06 g), compound **12** (0.1 g), and DIPEA (0.04 g) were added to 2 mL DMF, the mixture was reacted at room temperature for 24 h, and the $(N(EB)_2)$ **1** was purified and freeze-dried. The exact molecular weight of $N(tEB)_2$ **1** was 1539.4 g/mol.

Synthesis of $N(tEB)_2$ 2. To a 20 mL glass vial containing 100.0 mg of *o*-tolidine and 200.0 mg of NOTA-3HCl in 4 mL of DMSO was added 100 μL diisopropylethylamine and 90 μL diethyl cyanophosphonate. The mixture was stirred at room temperature overnight. The mixture was then purified with semipreparative HPLC. The peak containing the desired product was collected and the solution was frozen over dry ice and lyophilized overnight to give 28.5 mg pure tolidine-NOTA-tolidine (compound **13**). To a 20 mL glass vial containing 12.7 mg of tolidine-NOTA-tolidine in 1.0 mL of water was added 110 μmol of HCl (11 μL). The mixture was cooled in ice bath and 7.6 mg of sodium nitrite (110 μmol) in 0.5 mL of water was added to the vial dropwise. The mixture was stirred in ice bath for 20 min and the yellow diazonium salt solution (compound **14**) was added dropwise to another vial in ice bath containing 20.0 mg of 1-amino-8-naphthol-2,4-disulfonic acid and 13.0 mg of sodium bicarbonate in 0.5 mL of water. The mixture was stirred in ice bath for 3 h and purified with semipreparative HPLC. The product was collected and lyophilized overnight to give 15.0 mg pure NOTA-$N(tEB)_2$ (compound **15**). To a 20 mL glass vial containing 12.0 mg of NOTA-$N(tEB)_2$ and 11 mg of *N*-(2-aminoethyl)maleimide in 4 mL of DMF was added 20 mg of HATU and 50 μL DIPEA. The mixture was stirred at room temperature for 2 h and purified with HPLC to give 8.5 mg of maleimide-$N(tEB)_2$ ($N(tEB)_2$ 2) after lyophilization.

Synthesis of $N(tEB)_2$-Exendin-4. The $N(tEB)_2$-exendin-4 was obtained by mixing 2.26 mg of cys-40-exendin-4 and 0.78 mg of maleimide-$N(tEB)_2$ in 1 mL of water. The LC-MS analysis showed formation of the desired product.

Atomic Force Microscopy and Quantification. NtEB and $N(tEB)_2$ were, respectively, incubated with HSA (molar ratio of 1:10, 1:1, and 10:1) at room temperature for 30 min. Samples (10 μL) were cast on freshly peeled mica substrate, followed by drying, rinsing, and dehumidifying. AFM was carried out in tapping mode in air on a PicoForce Multimode AFM (Bruker, CA) equipped with a Nanoscope V controller, a type E scanner head, and a sharpened TESP-SS (Bruker, CA) AFM cantilever. An inverted optical microscope (IX71, Olympus, Japan) was used to capture pictures. AFM images were then analyzed by Nanoscope Software (v 7.3−8.15, Bruker, CA). For quantification, 10 different fields of view in one image were selected to quantify the "dimer" and the "monomer". The size and morphology of dimer (length: >25 nm, dumbbell-shaped) and monomer (length: ≤25 nm, width: ≤25 nm, no dumbbell-shaped structure) was defined by ImageJ (NIH, MD).

Kinetic Binding Assay. Binding affinity of EB, NtEB, $N(tEB)_2$, NtEB-exendin-4, and $N(tEB)_2$-exendin-4 with albumin was determined by biolayer interferometry (BLI) by interaction with biotinylated BSA/streptavidin biosensors using an Octet Red96 system (fortéBio), respectively. The dilution series of the compounds (100, 50, 25, 12.5, 6.25, 3.125, 1.526 μM) and PBS were used to delineate binding profile. The assay protocol was briefly described as follows. After washing with 1 × PBS for 60 s, biotinylated BSA (1 μg/mL) was loaded to the biosensor for 600 s, and after another 60 s washing, quenching with biocytin was performed for 180 s. Followed by another 60 s washing, association for 600 s and dissociation for another 600 s were performed in turn. Data was calculated and analyzed using Octet Analysis software v 7.0.

Preparation of ^{64}Cu Labeled NtEB, $N(tEB)_2$. Radionuclide ^{18}F and ^{64}Cu were produced and supplied by the Clinical Center's cyclotron facility in National Institute of Health (NIH). The method and procedure for preparation ^{18}F or ^{64}Cu labeled $N(tEB)_2$ followed the NtEB labeling procedure which had been reported in our previous study.[21] Specifically, $^{64}CuCl_2$ was converted to ^{64}Cu-acetate by adding 0.5 mL of 0.4 M NH_4OAc solution (pH 5.6) to 20 μL $^{64}CuCl_2$. ^{64}Cu-acetate solution (0.1 mL; 3−4 mCi) was added into a solution of 100 μg of NtEB or $N(tEB)_2$ in water (10 mg/mL). The mixtures were put on the orbital shaker (250 rpm) for 0.5 h at 37 °C. Then, the radiochemical purity was determined using iTLC plates (Fisher Scientific), developed in 0.1 M citric acid (pH 5). NtEB and $N(tEB)_2$ were purified by a C18 Sep-Pak (BOND-ELUT 100 mg, Varian), followed by elution from the cartridge using 70% ethanol and 30% PBS.

Cell Culture. U-87MG (human glioblastoma) and INS-1 (rat insulinoma) were purchased from American Type Culture Collection (ATCC, Rockville, MD), and UM-22B (human head and neck squamous carcinoma) cells were purchased from EMD Millipore (Billerica, MA). The cells were cultured

DOI: 10.1021/acs.bioconjchem.9b00258
Bioconjugate Chem. 2019, 30, 1711−1723

in Minimum Essential Medium (MEM), RPMI-1640 medium, and Dulbecco's modified Eagle medium (DMEM) respectively, containing 10% fetal bovine serum (Gibco) in cell incubator (a humidified atmosphere containing 5% CO_2 at 37 °C). The cells were passaged 2−3 times per week.

Animal Models. All the animal protocols were approved by the NIH Clinical Center Animal Care and Use Committee (ACUC). The studies for in vivo pharmacokinetics were performed in normal BALB/c mice (female; age, 6−8 weeks; weight, 18−20 g) (Harlan). For mouse xenograft model, female nude mice (6−8 weeks, 20−23 g) (Harlan) were inoculated on their right shoulder with 5×10^6 cells of U-87MG, INS-1, or UM-22B cells in Matrigel (Sigma) and PBS with volume ratio of 1:1, respectively.

PET Imaging. All PET images were acquired using an Inveon PET scanner (Siemens Preclinical Solutions, Malvern, PA). Mice were anesthetized using isoflurane/O_2 (2% v/v) before injection. For the in vivo pharmacokinetics study, healthy BALB/c mice (5 mice in each group) were administered 3.7 MBq (100 μCi) ^{18}F labeled NtEB or N(tEB)$_2$ via tail vein injection and 60 min dynamic PET acquisitions were performed. For the lymph node mapping study, 0.37 MBq/^{18}F labeled NtEB or N(tEB)$_2$ in 10 μL saline was injected into the footpad of the mice (5 mice in each group) (Siemens Medical Solutions, Malvern, PA). 60 min dynamic PET acquisitions were performed, and additional static PET images were acquired at 90 and 120 min p.i. For the tumor uptake study, PET scans were performed at 22−28 days post inoculation when the tumor volume reached about 200−300 mm^3. 3.7 MBq ^{64}Cu labeled NtEB or N(tEB)$_2$ were injected to nude mice (5−6 mice in per group) via tail vein and PET images were acquired 4, 24, and 48 h p.i. PET images were reconstructed without correction for attenuation or scattering using a three-dimensional ordered subsets expectation maximization algorithm. ASI Pro VMTM software was used for image analysis. Regions of interest (ROI) were drawn on LNs to calculate the %ID/g.

Comparison of the half-life of the N(tEB)$_2$ and NtEB through two-phase linear regression of the time activity curves over heart at various time points, respectively. The details were showed in the reported work,[60] and the data was calculated through GraphPad Prism v 7.03 (GraphPad Software Inc., San Diego, CA).

The above mice were killed at specified time points. Organs and blood were collected and wet weighed. The collected organs and blood, together with a series of standard solutions, were measured for ^{64}Cu radioactivity on a gamma counter (Wallac Wizard 1480, PerkinElmer). The radioactivity of organs and blood was converted to calculate the percentages of the injected dose (%ID) in organs of interest and the percentages of the injected dose per gram of tissue (%ID/g).

Enzymatic Degradation. For the enzymatic degradation setup, 80 μL exendin-4 (0.5 mg/mL) was incubated with trypsin (0.05 mg/mL) for different time (0, 5, 20, and 40 min) at 37 °C on orbital shaker (250 rpm). Before subjection to trypsin, the freshly prepared mixture of CH_3CN (75%) and formic acid (4%) was used as the stop solution for enzymatic reaction. The whole reaction solution was analyzed and most dominant fragments were assigned to specific molecules. For evaluating antidegradation effect, 80 μL free exendin-4, NtEB-exendin-4, and N(tEB)$_2$-exendin-4 were preincubated with HSA (20 mg/mL) for 30 min at 37 °C on the orbital shaker (250 rpm). The molar ratio of compound to HSA was optimized to 1:5. Before subjection to trypsin, the freshly prepared mixture of CH_3CN (75%) and formic acid (4%) was used as the stop solution for enzymatic reaction. The samples were subjected to trypsin (optimized to 0.05 mg/mL) digestion. 30 μL of sample at various time points (0, 5, 10, 20, 30, 50 min post treatment) was transferred into a 1.5 mL tube, and then 30 μL of stop solution was immediately added to each tube to stop the reaction. The samples (60 μL in total) were put in a dry ice box. Before LC/MS, all the samples were thawed to room temperature.

Qualitative LC/MS. Waters LC/MS system (Waters, Milford, MA) was employed with an Acquity UPLC system coupled to the Waters Q-Tof Premier high-resolution mass spectrometer. An Acquity BEH Shield RP18 column (150 mm × 2.1 mm) was eluted with a two-solution gradient of solution A (2 mM ammonium formate, 0.1% formic acid, and 5% CH_3CN) and solution B (2 mM ammonium formate and 0.1% formic acid in CH_3CN). The elution profile at 0.2 mL/min was as follows: 100% (v/v) A and 0% B initially, gradient from 0% to 40% B over 5 min, isocratic elution at 40% B for an additional 5 min, washing with 100% B over 2 min, and re-equilibrium with A for an additional 4 min. The injection volume was 10 μL. The entire column elute was introduced into the Q-Tof mass spectrometer. Ion detection was achieved in ESI mode using a source capillary voltage of 3.5 kV, source temperature of 100 °C, desolvation temperature of 200 °C, cone gas flow of 50 L/h (N_2), and desolvation gas flow of 700 L/h (N_2).

Quantitative LC/MS. For quantitative analysis of fragments from the enzymatic reaction, the LC/MS system consisted of an Agilent 1200 autosampler, Agilent 1200 LC pump, and an AB/MDS Sciex 4000 Q TRAP (Life Technologies Corporation, Carlsbad, California). Separation was achieved on an Phenomenex Gemini column (5 μm, 110A, 50 mm × 4.6 mm) with 2 mM ammonium acetate and CH_3CN with the following gradient system at a flow rate of 1.0 mL/min: 100% (v/v) A and 0% B for 1 min initially, gradient from 0% to 46% B over 4 min, isocratic elution at 46% B for an additional 5 min, washing with 100% B over 1 min, and re-equilibrium with A for an additional 1 min. Different combinations of multiple-reaction monitoring (MRM) and full scan MS/MS experiments were performed. Three replicate injections (10 μL) were made for each time-point metabolite. The specific comparisons made for quantitation used a single MRM transition per analyte.

Hypoglycemic Efficacy and in Vivo Pharmacokinetics. Hypoglycemic efficacy of N(tEB)$_2$-exendin-4 were evaluated using a glucose tolerance test in male db/db mice (6−8 weeks), Saline, exendin-4, NtEB-exendin-4, and commercially available hypoglycemic drug semaglutide were used as control. Under nonfasting conditions with free access to food and water, animals were administrated with a single dose of subcutaneous injection of saline, exendin-4, semaglutide, NtEB-exendin-4, or N(tEB)$_2$-exendin-4 (25 nmol/kg body weight, n = 3/group). Blood samples were collected from tail vein at different time points (0, 15, 30, 60, 90, 120 min) post administration, and blood glucose levels were monitored with a blood glucose meter (ACCU-CHEK Sensor, Roche Diagnostics Corp., USA).

Plasma Exendin-4 levels were determined by a commercial Exendin-4 ELISA kit (Phoenix Biotech, USA) according to the manufacturer's instructions. Briefly, 25 μL blood samples collected at different time points from the mice were added

DOI: 10.1021/acs.bioconjchem.9b00258
Bioconjugate Chem. 2019, 30, 1711−1723

to the microwells of the plate, after incubation and washing, 100 μL SA-HRP was added to each well and incubated them for 1 h. The solution was removed and washed, followed by TMB substrate solution adding to each well. Then, 100 μL HCl was added to stop the reaction. The results were observed by a Microplate Reader.

Statistical Analysis. Quantitative data were expressed as means ± st.d. (the standard deviation). Analyses were performed by SPSS software v 13.0 (SPSS, Chicago, IL). Two-tailed unpaired Student's t tests were used to test the differences between two groups. One-way ANOVA with Bonferroni post test was used to compare the differences between three or more groups. Slope values for blood (K_α and K_β) TACs were calculated from either dynamic or multipoint static PET scans using linear regression. For comparison of the half-live of NtEB and N(tEB)$_2$, two-phase linear regression was performed by GraphPad Prism v 7.03 (GraphPad Software Inc., San Diego, CA). p values of <0.05 were considered statistically significant. (***p < 0.001, *p < 0.05, ns: not significant (p > 0.05).)

■ ASSOCIATED CONTENT

Supporting Information

The Supporting Information is available free of charge on the ACS Publications website at DOI: 10.1021/acs.bioconjchem.9b00258.

Design and screening of the optimal N(tEB)$_2$, including modeling of simulation and experimental characterization; synthesis and characterization, improved pharmacokinetics, and enhanced tumor retention of N(tEB)$_2$; chemical synthesis and characterization of N(tEB)$_2$-exendin-4; data tables (PDF)

Binding sites of N(tEB)$_2$ for albumin (MP4)

Binding pose of N(tEB)$_2$-albumins dimer (MP4)

■ AUTHOR INFORMATION

Corresponding Authors

*E-mail: shoujun.zhu@nih.gov.
*E-mail: gang.niu@nih.gov.
*E-mail: shawn.chen@nih.gov.

ORCID

Yi Liu: 0000-0001-5008-1097
Gang Liu: 0000-0003-2613-7286
Xiaoyuan Chen: 0000-0002-9622-0870

Notes

The authors declare no competing financial interest.

■ ACKNOWLEDGMENTS

This work was supported by the Intramural Research Program of the National Institute of Biomedical Imaging and Bioengineering (NIBIB), National Institutes of Health (NIH), and the National Natural Science Foundation of China (81871404).

■ REFERENCES

(1) Mitragotri, S., Burke, P. A., and Langer, R. (2014) Overcoming the cCallenges in Administering Biopharmaceuticals: Formulation and Delivery Strategies. *Nat. Rev. Drug Discovery 13*, 655−672.

(2) Sleep, D., Cameron, J., and Evans, L. R. (2013) Albumin as a Versatile Platform for Drug Half-Life Extension. *Biochim. Biophys. Acta, Gen. Subj. 1830*, 5526−5534.

(3) Liu, H., Moynihan, K. D., Zheng, Y., Szeto, G. L., Li, A. V., Huang, B., Van Egeren, D. S., Park, C., and Irvine, D. J. (2014) Structure-Based Programming of Lymph-Node Targeting in Molecular Vaccines. *Nature 507*, 519−522.

(4) Larsen, M. T., Kuhlmann, M., Hvam, M. L., and Howard, K. A. (2016) Albumin-Based Drug Delivery: Harnessing Nature to Cure Disease. *Mol. Cell Ther. 4*, 3.

(5) Marso, S. P., Bain, S. C., Consoli, A., Eliaschewitz, F. G., Jódar, E., Leiter, L. A., Lingvay, I., Rosenstock, J., Seufert, J., Warren, M. L., et al. (2016) Semaglutide and Cardiovascular Outcomes in Patients with Type 2 Diabetes. *N. Engl. J. Med. 375*, 1834−1844.

(6) Zhu, G., Lynn, G. M., Jacobson, O., Chen, K., Liu, Y., Zhang, H., Ma, Y., Zhang, F., Tian, R., Ni, Q., et al. (2017) Albumin/Vaccine Nanocomplexes that Assemble *In Vivo* for Combination Cancer Immunotherapy. *Nat. Commun. 8*, 1954.

(7) Myers, S. R., Yakubu-Madus, F. E., Johnson, W. T., Baker, J. E., Cusick, T. S., Williams, V. K., Tinsley, F. C., Kriauciunas, A., Manetta, J., and Chen, V. J. (1997) Acylation of Human Insulin with Palmitic Acid Extends the Time Action of Human Insulin in Diabetic Dogs. *Diabetes 46*, 637−642.

(8) Yoon, H. J., Kang, K. W., Chun, I. K., Cho, N., Im, S. A., Jeong, S., Lee, S., Jung, K. C., Lee, Y. S., Jeong, J. M., et al. (2014) Correlation of Breast Cancer Subtypes, Based on Estrogen Receptor, Progesterone Receptor, and HER2, with Functional Imaging Parameters from (68)Ga-RGD PET/CT and (18)F-FDG PET/CT. *Eur. J. Nucl. Med. Mol. Imaging 41*, 1534−1543.

(9) Lee, J., Lee, C., Kim, I., Moon, H. R., Kim, T. H., Oh, K. T., Lee, E. S., Lee, K. C., and Youn, Y. S. (2012) Preparation and Evaluation of Palmitic Acid-Conjugated Exendin-4 with Delayed Absorption and Prolonged Circulation for Longer Hypoglycemia. *Int. J. Pharm. 424*, 50−57.

(10) Moynihan, K. D., Opel, C. F., Szeto, G. L., Tzeng, A., Zhu, E. F., Engreitz, J. M., Williams, R. T., Rakhra, K., Zhang, M. H., and Rothschilds, A. M. (2016) Eradication of Large Established Tumors in Mice by Combination Immunotherapy that Engages Innate and Adaptive Immune Responses. *Nat. Med. 22*, 1402−1410.

(11) Koehler, M. F., Zobel, K., Beresini, M. H., Caris, L. D., Combs, D., Paasch, B. D., and Lazarus, R. A. (2002) Albumin Affinity Tags Increase Peptide Half-Life *In Vivo*. *Bioorg. Med. Chem. Lett. 12*, 2883−2886.

(12) Dumelin, C. E., Trüssel, S., Buller, F., Trachsel, E., Bootz, F., Zhang, Y., Mannocci, L., Beck, S. C., Drumea-Mirancea, M., Seeliger, M. W., et al. (2008) A Portable Albumin Binder From a DNA-Encoded Chemical Library. *Angew. Chem. 120*, 3240−3245.

(13) Dennis, M. S., Zhang, M., Meng, Y. G., Kadkhodayan, M., Kirchhofer, D., Combs, D., and Damico, L. A. (2002) Albumin Binding as a General Strategy for Improving the Pharmacokinetics of Proteins. *J. Biol. Chem. 277*, 35035−35043.

(14) Rousseau, E., Lau, J., Zhang, Z., Uribe, C. F., Kuo, H.-T., Zhang, C., Zeisler, J., Colpo, N., Lin, K.-S., and Bénard, F. (2018) Effects of adding an albumin binder chain on [177Lu]Lu-DOTATATE. *Nucl. Med. Biol. 66*, 10−17.

(15) Wang, Z., Tian, R., Niu, G., Ma, Y., Lang, L., Szajek, L. P., Kiesewetter, D. O., Jacobson, O., and Chen, X. (2018) Single Low-Dose Injection of Evans Blue Modified PSMA-617 Radioligand Therapy Eliminates Prostate-Specific Membrane Antigen Positive Tumors. *Bioconjugate Chem. 29*, 3213−3221.

(16) Hopp, J., Hornig, N., Zettlitz, K. A., Schwarz, A., Fuss, N., Muller, D., and Kontermann, R. E. (2010) The Effects of Affinity and Valency of an Albumin-Binding Domain (ABD) on the Half-Life of a Single-Chain Diabody-ABD Fusion Protein. *Protein Eng., Des. Sel. 23*, 827−834.

(17) Langenheim, J. F., and Chen, W. Y. (2009) Improving the Pharmacokinetics/Pharmacodynamics of Prolactin, GH, and Their Antagonists by Fusion to a Synthetic Albumin-Binding Peptide. *J. Endocrinol. 203*, 375−387.

(18) Gibson, J. G., and Evans, W. A. (1937) Clinical Studies of the Blood Volume. I. Clinical Application of a Method Employing the

DOI: 10.1021/acs.bioconjchem.9b00258
Bioconjugate Chem. 2019, 30, 1711−1723

Azo Dye "Evans Blue" and the Spectrophotometer. *J. Clin. Invest. 16*, 301−316.
(19) Louveau, A., Smirnov, I., Keyes, T. J., Eccles, J. D., Rouhani, S. J., Peske, J. D., Derecki, N. C., Castle, D., Mandell, J. W., Lee, K. S., et al. (2015) Structural and functional features of central nervous system lymphatic vessels. *Nature 523*, 337−341.
(20) Thurston, G., Suri, C., Smith, K., McClain, J., Sato, T., Yancopoulos, G., and McDonald, D. (1999) Leakage-Resistant Blood Vessels in Mice Transgenically Overexpressing Angiopoietin-1. *Science 286*, 2511−2514.
(21) Niu, G., Lang, L., Kiesewetter, D. O., Ma, Y., Sun, Z., Guo, N., Guo, J., Wu, C., and Chen, X. (2014) *In vivo* Labeling of Serum Albumin for PET. *J. Nucl. Med. 55*, 1150−1156.
(22) Wang, Y., Lang, L., Huang, P., Wang, Z., Jacobson, O., Kiesewetter, D. O., Ali, I. U., Teng, G., Niu, G., and Chen, X. (2015) *In vivo* Albumin Labeling and Lymphatic Imaging. *Proc. Natl. Acad. Sci. U. S. A. 112*, 208−213.
(23) Chen, H., Jacobson, O., Niu, G., Weiss, I. D., Kiesewetter, D. O., Liu, Y., Ma, Y., Wu, H., and Chen, X. (2017) Novel "Add-On" Molecule Based on Evans Blue Confers Superior Pharmacokinetics and Transforms Drugs to Theranostic Agents. *J. Nucl. Med. 58*, 590−597.
(24) Tian, R., Jacobson, O., Niu, G., Kiesewetter, D. O., Wang, Z., Zhu, G., Ma, Y., Liu, G., and Chen, X. (2018) Evans Blue Attachment Enhances Somatostatin Receptor Subtype-2 Imaging and Radiotherapy. *Theranostics 8*, 735−745.
(25) Zhang, J., Wang, H., Jacobson, O. W., Cheng, Y., Niu, G., Li, F., Bai, C., Zhu, Z., and Chen, X. (2018) Safety, Pharmacokinetics and Dosimetry of a Long-Acting Radiolabeled Somatostatin Analogue 177Lu-DOTA-EB-TATE in Patients with Advanced Metastatic Neuroendocrine Tumors. *J. Nucl. Med. 59*, 1699−1705.
(26) Liu, Y., Wang, G., Zhang, H., Ma, Y., Lang, L., Jacobson, O., Kiesewetter, D. O., Zhu, L., Gao, S., Ma, Q., et al. (2016) Stable Evans Blue Derived Exendin-4 Peptide for Type 2 Diabetes Treatment. *Bioconjugate Chem. 27*, 54−58.
(27) Chen, H., Wang, G., Lang, L., Jacobson, O., Kiesewetter, D. O., Liu, Y., Ma, Y., Zhang, X., Wu, H., Zhu, L., et al. (2016) Chemical Conjugation of Evans Blue Derivative: A Strategy to Develop Long-Acting Therapeutics through Albumin Binding. *Theranostics 6*, 243−253.
(28) Mammen, M., Choi, S. K., and Whitesides, G. M. (1998) Polyvalent Interactions in Biological Systems: Implications for Design and Use of Multivalent Ligands and Inhibitors. *Angew. Chem., Int. Ed. 37*, 2754−2794.
(29) Muñoz, A., Sigwalt, D., Illescas, B. M., Luczkowiak, J., Rodríguez-Pérez, L., Nierengarten, I., Holler, M., Remy, J.-S., Buffet, K., Vincent, S. P., et al. (2016) Synthesis of Giant Globular Multivalent Glycofullerenes as Potent Inhibitors in a Model of Ebola Virus Infection. *Nat. Chem. 8*, 50−57.
(30) Whitesides, G. M., and Grzybowski, B. (2002) Self-Assembly at All Scales. *Science 295*, 2418−2421.
(31) Kostiainen, M. A., Kasyutich, O., Cornelissen, J. J., and Nolte, R. J. (2010) Self-Assembly and Optically Triggered Disassembly of Hierarchical Dendron−Virus Complexes. *Nat. Chem. 2*, 394−399.
(32) Liu, Z., and Chen, X. (2016) Simple Bioconjugate Chemistry Serves Great Clinical Advances: Albumin as a Versatile Platform for Diagnosis and Precision Therapy. *Chem. Soc. Rev. 45*, 1432−1456.
(33) Friedrichs, B. (1997) *Th. Peters. Jr.: All about Albumin. Biochemistry, Genetics, and Medical Applications*, Academic Press, Inc., San Diego, CA.
(34) Ghuman, J., Zunszain, P. A., Petitpas, I., Bhattacharya, A. A., Otagiri, M., and Curry, S. (2005) Structural Basis of the Drug-Binding Specificity of Human Serum Albumin. *J. Mol. Biol. 353*, 38−52.
(35) Freedman, F. B., and Johnson, J. A. (1969) Equilibrium and Kinetic Properties of the Evans Blue-Albumin System. *Am. J. Physiol. 216*, 675−681.
(36) Trott, O., Olson, A. J., et al. (2009) AutoDock Vina: Improving the Speed and Accuracy of Docking with a New Scoring Function, Efficient Optimization, and Multithreading. *J. Comput. Chem. 31*, 455−461.
(37) Wang, Z., Sun, H., Yao, X., Li, D., Xu, L., Li, Y., Tian, S., and Hou, T. (2016) Comprehensive Evaluation of Ten Docking Programs on a Diverse Set of Protein−Ligand Complexes: the Prediction Accuracy of Sampling Power and Scoring Power. *Phys. Chem. Chem. Phys. 18*, 12964−12975.
(38) Illing, P. T., Vivian, J. P., Dudek, N. L., Kostenko, L., Chen, Z., Bharadwaj, M., Miles, J. J., Kjer-Nielsen, L., Gras, S., Williamson, N. A., et al. (2012) Immune Self-Reactivity Triggered by Drug-Modified HLA-Peptide Repertoire. *Nature 486*, 554−558.
(39) Chu, C. T., Ji, J., Dagda, R. K., Jiang, J. F., Tyurina, Y. Y., Kapralov, A. A., Tyurin, V. A., Yanamala, N., Shrivastava, I. H., Mohammadyani, D., et al. (2013) Cardiolipin Externalization to the Outer Mitochondrial Membrane Acts as an Elimination Signal for Mitophagy in Neuronal Cells. *Nat. Cell Biol. 15*, 1197−1205.
(40) Penchala, S. C., Miller, M. R., Pal, A., Dong, J., Madadi, N. R., Xie, J., Joo, H., Tsai, J., Batoon, P., Samoshin, V., et al. (2015) A Biomimetic Approach for Enhancing the *In vivo* Half-Life of Peptides. *Nat. Chem. Biol. 11*, 793−798.
(41) Chen, Z., Wang, Z., and Gu, Z. (2019) Bioinspired and Biomimetic Nanomedicines. *Acc. Chem. Res.*, DOI: 10.1021/acs.accounts.9b00079.
(42) Pratley, R. E., Aroda, V. R., Lingvay, I., Lüdemann, J., Andreassen, C., Navarria, A., and Viljoen, A. (2018) Semaglutide Versus Dulaglutide Once Weekly in Patients with Type 2 Diabetes (SUSTAIN 7): A Randomised, Open-Label, Phase 3b Trial. *Lancet Diabetes Endocrinol. 6*, 275−286.
(43) Scheen, A. J. (2017) Semaglutide: a Promising New Glucagon-Like Peptide-1 Receptor Agonist. *Lancet Diabetes Endocrinol. 5*, 236−238.
(44) Gilson, M. K., Given, J. A., Bush, B. L., and McCammon, J. A. (1997) The Statistical-Thermodynamic Basis for Computation of Binding Affinities: A Critical Review. *Biophys. J. 72*, 1047−1069.
(45) Lee, F. S., Chu, Z. T., Bolger, M. B., and Warshel, A. (1992) Calculations of Antibody-Antigen Interactions: Microscopic and Semi-Microscopic Evaluation of the Free Energies of Binding of Phosphorylcholine Analogs to McPC603. *Protein Eng., Des. Sel. 5*, 215−228.
(46) Lee, J., Tofoleanu, F., Pickard, F. C. t., Konig, G., Huang, J., Damjanovic, A., Baek, M., Seok, C., and Brooks, B. R. (2017) Absolute Binding Free Energy Calculations of CBClip Host-Guest Systems in the SAMPL5 Blind Challenge. *J. Comput.-Aided Mol. Des. 31*, 71−85.
(47) Straatsma, T., and Berendsen, H. (1988) Free Energy of Ionic Hydration: Analysis of a Thermodynamic Integration Technique to Evaluate Free Energy Differences by Molecular Dynamics Simulations. *J. Chem. Phys. 89*, 5876−5886.
(48) Chipot, C., and Pohorille, A. (2007) *Free Energy Calculations*, Springer, Berlin, Heidelberg.
(49) Fukunishi, H., Watanabe, O., and Takada, S. (2002) On the Hamiltonian Replica Exchange Method for Efficient Sampling of Biomolecular Systems: Application to Protein Structure Prediction. *J. Chem. Phys. 116*, 9058−9067.
(50) Itoh, S. G., and Okumura, H. (2013) Hamiltonian Replica-Permutation Method and Its Applications to an Alanine Dipeptide and Amyloid-β(29−42) Peptides. *J. Comput. Chem. 34*, 2493−2497.
(51) Lee, J., Miller, B. T., Damjanovic, A., and Brooks, B. R. (2014) Constant pH Molecular Dynamics in Explicit Solvent with Enveloping Distribution Sampling and Hamiltonian Exchange. *J. Chem. Theory Comput. 10*, 2738−2750.
(52) Konig, G., and Brooks, B. R. (2012) Predicting Binding Affinities of Host-Guest Systems in the SAMPL3 Blind Challenge: The Performance of Relative Free Energy Calculations. *J. Comput.-Aided Mol. Des. 26*, 543−550.
(53) Bennett, C. H. (1976) Efficient Estimation of Free Energy Differences from Monte Carlo Data. *J. Comput. Phys. 22*, 245−268.

DOI: 10.1021/acs.bioconjchem.9b00258
Bioconjugate Chem. 2019, 30, 1711−1723

(54) König, G., and Boresch, S. (2011) Non-Boltzmann Sampling and Bennett's Acceptance Ratio Method: How to Profit From Bending the Rules. *J. Comput. Chem. 32*, 1082−1090.
(55) Bhattacharya, A. A., Curry, S., and Franks, N. P. (2000) Binding of the General Anesthetics Propofol and Halothane to Human Serum Albumin: High Resolution Crystal Structures. *J. Biol. Chem. 275*, 38731−38738.
(56) Brooks, B. R., Brooks, C. L., Mackerell, A. D., Jr., Nilsson, L., Petrella, R. J., Roux, B., Won, Y., Archontis, G., Bartels, C., Boresch, S., et al. (2009) CHARMM: The Biomolecular Simulation Program. *J. Comput. Chem. 30*, 1545−1614.
(57) Trott, O., and Olson, A. J. (2009) AutoDock Vina: Improving the Speed and Accuracy of Docking with a New Scoring Function, Efficient Optimization, and Multithreading. *J. Comput. Chem. 31*, 455−461.
(58) Schrödinger, L. (2015) *PyMOL Molecular Graphics System*, v 1.8, Schrödinger, LLC.
(59) Vanommeslaeghe, K., Hatcher, E., Acharya, C., Kundu, S., Zhong, S., Shim, J., Darian, E., Guvench, O., Lopes, P., Vorobyov, I., et al. (2009) CHARMM General Force Field: A Force Field for Drug-Like Molecules Compatible with the CHARMM All-Atom Additive Biological Force Fields. *J. Comput. Chem. 31*, 671−690.
(60) Yu, M., and Zheng, J. (2015) Clearance Pathways and Tumor Targeting of Imaging Nanoparticles. *ACS Nano 9*, 6655−6674.

DOI: 10.1021/acs.bioconjchem.9b00258
Bioconjugate Chem. 2019, 30, 1711−1723